Supplementary Information Appendix for:

Background-suppressed tumor-targeted photoacoustic imaging using bacterial carriers

Rongkang Gao[a#], Feng Liu[a#], Wenfeng Liu[a], Silue Zeng[a, c], Jingqin Chen[a], Ruru Gao[b], Liang Wang[a], Chihua Fang[c], Liang Song[a], Adam C. Sedgwick,[d] Jonathan L. Sessler[d]*, Jun Chu[a]*, Fei Yan[b]*, Chengbo Liu[a]*

Corresponding authors: Chengbo Liu; Fei Yan; Jun Chu; Jonathan L. Sessler

E-mail: *cb.liu@siat.ac.cn; fei.yan@siat.ac.cn; jun.chu@siat.ac.cn; sessler@cm.utexas.edu*

Supplemental Methods 1: Structural organization and plasmid construction of new genetically encoded probes

New photoswitchable chromoproteins, including m*Dr*BphP-PCMm, m*Dr*BphP-PCMm/F469W and m*Dr*BphP-PCMm/L463R, were constructed on the basis of *Dr*BphP-PCM, as depicted in Fig. 1A. For the construction of monomeric *Dr*BphP-PCM (i.e., m*Dr*BphP-PCMm), F145S, L311E and L314E mutations were introduced by overlap extension polymerase chain reaction (PCR) [1]. The

constructed plasmid was named pJC-m*Dr*BphP-PCMm-HO. To engineer m*Dr*BphP-PCMm/F469W and m*Dr*BphP-PCMm/L463R, mutations (F469W or L463R) were introduced into m*Dr*BphP-PCMm to construct these two PA probes by overlap extension PCR [2]. In this study, the *Dr*BphP-PCM gene was synthesized by GenScript Biotech Corp. (Nanjing China). The *Dr*BphP-PCM gene was PCR amplified using PrimerSTAR Max DNA polymerase (Takara) and ligated into the constitutive bacterial expression vector pNCS at the KpnI/EcoRI site using an In-Fusion HD Cloning Kit (Takara). For bacterial expression, the heme oxygenase-1 (HO) gene from *Synechocystis sp* was used*. The* PCC 6803 and EM7 promoters were PCR amplified, and the EM7-HO fragment was cloned into the pNCS plasmid at the Kpn2I/XhoI site. The final plasmid is referred to as pJC-*Dr*BphP-PCM-HO.

Supplemental Methods 2: Monomer formation

It has been reported [1] that three mutations at the dimerization interface of *Dr*BphP, F145S/L311E/L214E, can make *Dr*BphP-CBD (CBD domain of *Dr*BphP) monomeric. Consistent with this finding, our m*Dr*BphP-PCMm, which has the same mutations described above, behaved as a monomer (Fig. S2A), as did m*Dr*BphP-PCMm/F469W. This is different from the previously reported dimeric DrBphP (*Dr*BphP-PCM) or RpBphP1 proteins, making it a useful tag to label cellular proteins of interest.

To perform size exclusion liquid chromatography (Fig. S2A), 200 μL of purified m*Dr*BphP-PCMm, *Dr*BphP-PCM and mKate2 proteins (10 mg/mL) were loaded onto an HPLC column (GE Healthcare) equilibrated with PBS buffer, pH 7.0. A flow rate of 1 ml/min was used.

Supplemental Methods 3: Protein characterization

The absorption spectra of different genetically encoded probes, including m*Dr*BphP-PCMm/F469W, m*Dr*BphP-PCMm/L463R, m*Dr*BphP-PCMm, *Dr*BphP-PCM and RpBphP1, were all recorded using a standard UV–Vis spectrophotometer (Shimadzu UV-2700). For the ON/OFF state spectrum measurement, illumination at 630 nm/780 nm for 4-6 min was effected using custom-assembled LED arrays (Thorlabs LIU630A/LIU780A); this allowed each genetically encoded probe to be photoswitched to the corresponding ON/OFF state. After photoconversion, the LED light source was turned off before the measurement, such that the absorption spectroscopic measurements were independent of the dynamic process of photoswitching caused by the 630/780 nm light source. Owing to the extremely low light intensity (<1 μW/cm^2) of the UV–visible spectrophotometer, the spectral alteration caused by optical illumination inside the spectrophotometer can be neglected. Fig. 1B shows the absorption spectra of different genetically encoded probes in both the ON and OFF states; these correspond to the red and far-red states, respectively. The absorbance spectrum was normalized to the most intense peak within the spectral region of interest as shown in Fig. 1B.

Supplemental Methods 4: Fluorescent properties of m*Dr*BphP-PCMm/F469W

Stellar competent bacterial cells were transformed using the pcDNA3.1 vector (negative control), the pJC-m*Dr*BphP-PCMm/F469W-HO vector or the pJC-IFP2.0-HO vector and cultured overnight at 34 °C. Both m*Dr*BphP-PCMm/F469W and IFP2.0 (bright near infrared FP) are from *Dr*BphP. Then the cells were cultured at room temperature for 3 days. Bacterial cells expressing different proteins or negative control were harvested at the same number of cells, and were suspended in PBS buffer and centrifuged (Fig. S3). The pellets were used for fluorescent imaging using an IVIS

spectrum imaging system (PerkinElmer) with excitation and emission filters of 675/30 nm and 720/30 nm, respectively. The pellets were suspended in PBS and lysed by sonication followed by centrifugation. The fluorescence spectra of clear lysates were measured using an Infinite M1000 PRO fluorometer (Tecan).

Supplemental Methods 5: Animal preparation and cell culture

In this study, female BALB/c nude mice (6-8 weeks old and ~20−25 g weight, purchased from Beijing Vital River Laboratory Animal Technology Co., Ltd, China), were used for *in vivo* experiments. All animal experiments were performed in conformity with the guidelines approved by the Animal Study Committee of the Shenzhen Institutes of Advanced Technology, Chinese Academy of Sciences (Protocol number: SIAT-IACUC-210303-HCS-YF-A1693). Throughout the experiment, the mice were maintained under anesthesia using a mixture of vaporized isoflurane and oxygen (1 l/minute). The temperature of the mouse body was maintained at 37 °C using a temperature-controlled heating pad (RWD Life Science, Shenzhen, China).

For the breast tumor model, breast cancer cells (4T1, ~10^6) suspended in PBS (100 µL) were inoculated into the thighs of mice. The breast cancer cell line 4T1 was cultured in DMEM supplemented with 10% fetal bovine serum (FBS; Gibco, Australia) and 1% penicillin–streptomycin solution in a humidified incubator (5% CO_2, 37 °C).

Supplemental Methods 6: PACT imaging system

Fig. 2B provides a schematic view of the custom-built PACT system used in our study. An optical parametric oscillator (OPO) laser (Innolas GmbH, Bonn, Germany, 4–6 ns pulse duration) was employed for optical excitation within a tunable wavelength range extending from 680 nm to 980 nm with a repetition rate of 30 Hz. The laser pulse was attenuated by a combination of a half-wave plate and a Glan prism. Then, a convex lens was used to couple the laser beam to a multimode optical fiber with a 1500-µm core diameter through a fiber coupler. To ensure good overlap of the optical excitation and acoustic detection at the sample surface, the excitation light coming out of the optical fiber was reshaped by two cylindrical lenses (plano-convex and plano-concave cylindrical lenses, AYL1210-B and LK1006L1-B, Thorlabs, Newton, New Jersey) into a narrow rectangular pattern to fit the shape of the acoustic detection. With a pulse energy of 45 mJ and an illumination area of 2.5 cm^2 on the mouse tumor surface, the optical fluence on the mouse tumor surface was approximately 18 mJ/cm^2, which is below the safety limit (20 mJ/cm^2 at 780 nm wavelength) set by the American National Standards Institute (ANSI). The incident optical illumination on the mouse tumor and nearby regions generated PA signals, which were detected by a 128-element ultrasound linear-array transducer (center frequency: 15 MHz ± 10%, bandwidth >60% at -6 dB, Vermon). The detected signals were then transferred to the 128-channel data acquisition board integrated within the Verasonics Vantage ultrasound platform (Verasonics, Inc., Kirkland, Washington) for further processing. As shown in Fig. 2B, the signal trigger circuit was employed to synchronize both the laser firing of the OPO laser source and the signal acquisition of the Verasonics Vantage ultrasound platform. This ensures that the PA signals were acquired at a frame rate equal to the repetition rate of the pulse firing (30 Hz). An imaging speed (0.03 s per frame) was sufficient to capture the decay process of the PA signal of the gene reporters (m*Dr*BphP-PCMm/F469W) as a function of time (Fig. S2) when illuminated with the 780 nm wavelength. It is worth mentioning that during OPO laser firing, there exists a short period in which the laser pulse energy increases from zero to the desired value. We employed a laser shutter (LS-RS20) to deflect the incoming laser beam onto the imaging targets

during this unsteady period. After the laser energy reached steady state, the shutter was opened, and the laser beam passed through the shutter without interruption. This ensured that the PA signal in the time domain reflected only the photoswitching properties of the target and removed the influence of the unstable laser pulse energy. The laser shutter had an opening speed (2 ms), i.e., faster than the pulse-to-pulse interval (33 ms) of the laser, which help prevented accidental exposure of the protein to the laser beam during the shutter opening process; thus, the maximum PA signal corresponded to the first pulse illuminating the proteins and protein-expressing *E. coli* (Fig.S1B and C).

Supplemental Methods 7: Data processing

The PA raw data were reconstructed using a standard back-projection algorithm [3] to form a tomography PA image of the mouse tumor and nearby regions. The raw data for each animal at each time point were processed using MATLAB (R2017b) to show the Bscan image. Following the acquisition of the PA signals, our hybrid platform was used to acquire ultrasound images of the same area underneath the transducer to merge the PA and US images. For the statistical analysis of *E. coli* distributions in mice tumor regions, the PA signals were quantified based on the average values at randomly selected positions (at least 10 positions) in the tumor regions. The error bars indicate the standard error of PA signals for three mice used in PA imaging results. The above quantification procedures were also applied to the fluorescence signals in the FISH images of both the tumor regions and the normal organs (Fig. 6A and Fig. S13). The error bars indicate the standard error of the fluorescence intensity of the selected positions chosen for evaluation.

Supplemental Methods 8: Histological analysis

To confirm the presence of *E. coli* in the tumor region, FISH was applied for histological examination by using a DNA sequence of *E. coli* to target the complementary sequences and thereby identify the locations of *E. coli*. Before the FISH experiments, mice tumors were harvested and placed in fixation fluid (DEPC) for 24 h. Tissue samples were embedded in paraffin and sliced with a microtome. After dewaxing and dehydration, the standard FISH procedure was performed to detect the expression of *E. coli* in tumor tissues. The cell nuclei were counterstained by incubating the slices with DAPI for 8 min in the dark. To identify the FISH results, fluorescence microscopy was used for examination and photography. Nuclei stained with DAPI glow blue with ultraviolet excitation wavelengths of 330-380 nm and emission wavelengths of 420 nm. In contrast, *E. coli* glows green under excitation wavelengths of 465-495 nm and emission wavelengths of 515-555 nm. Furthermore, standard hematoxylin and eosin (H&E) staining was conducted on the adjacent slice of the same tumor sample to provide the cellular and tissue structure of the cancerous regions. FISH and H&E examinations were also conducted on different organs of mice to thoroughly assess the long-term distribution of *E. coli* in local organs (FISH), as well as the possible damage to normal organs and tissues (H&E staining). The H&E results were examined using bright-field microscopy (NanoZoomer, Hamamatsu) with a 20×/0.67-NA objective.

Figures S1-13

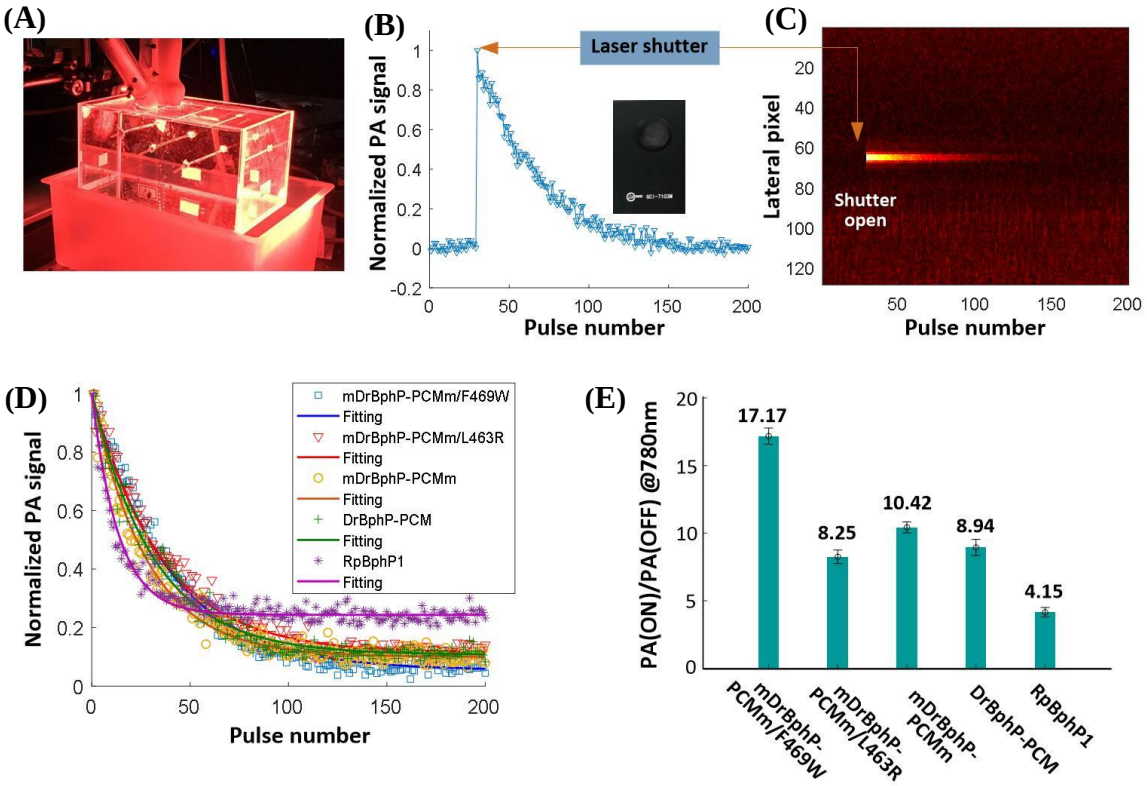

Fig. S1. Photoacoustic characterization of different purified proteins. (A) Experimental setup used for the characterization of different proteins. Plastic tubes were used for PA imaging. (B) Decrease in the PA signal of the protein as a function of time upon illumination at 780 nm. A laser shutter (LS-RS20) was employed to deflect the incoming laser beam during the unsteady state. The maximum PA signal was from the first pulse illuminating the protein. (C) Corresponding maximum amplitude projection (MAP) images of purified protein during 780 nm illumination, plotted against time, i.e., pulse number (X-axis), showing the variation in the PA signal during the photoswitching process from the ON to OFF states. (D) Normalized PA signal as a function of pulse number for five different proteins. To convert the pulse number into time (s), the *x*-axis in (B-D) should be multiplied by a factor of 0.033. (E) Photoswitching contrast, PA(ON)/PA(OFF) @780 nm, for five different proteins. Data are presented as the mean ± standard error. The results support the conclusion that m*Dr*BphP-PCMm/F469W outperforms the other chromoproteins considered in the present study.

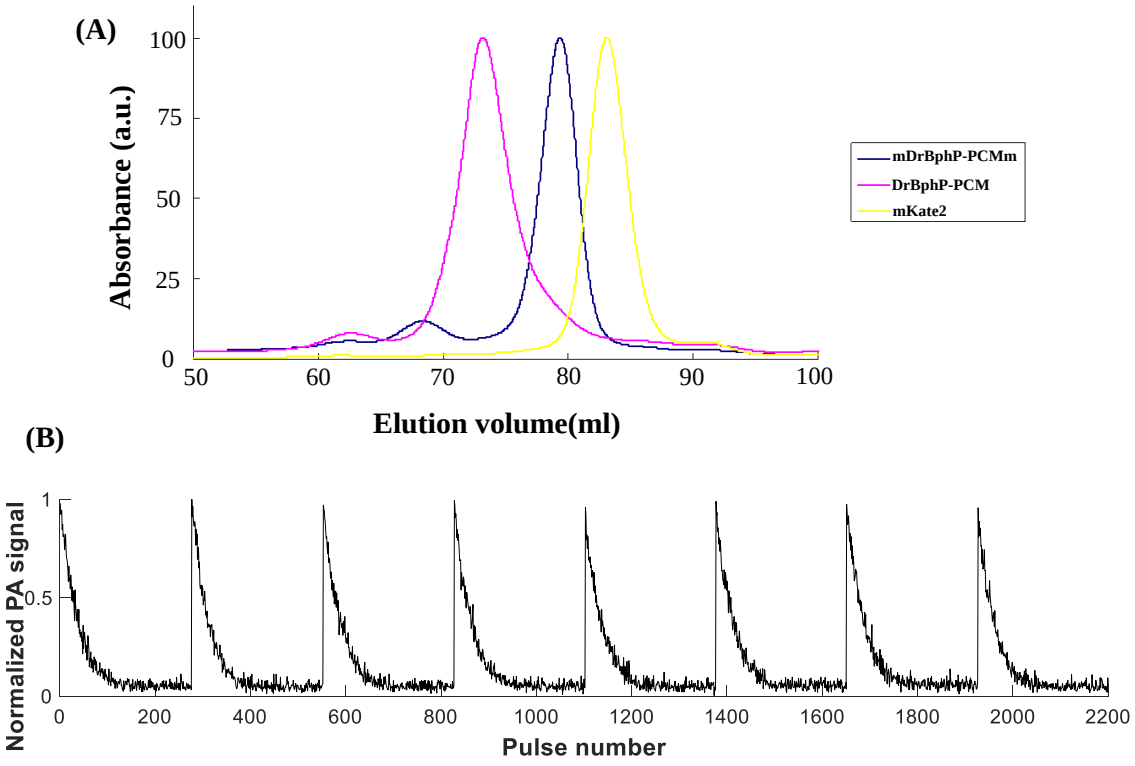

Fig. S2. The monomer behavior of m*Dr*BphP-PCMm and photoswitching cycles of m*Dr*BphP-PCMm/F469W. (A) Size exclusion chromatographic analyses of m*Dr*BphP-PCMm, *Dr*BphP-PCM and mKate2 at 10 mg/ml. (B) Multiple switching cycles induced by the consecutive switching between 780 nm and 630 nm photo-illumination. The results support the contention that m*Dr*BphP-PCMm/F469W is capable of undergoing robust reversible photoswitching. To convert the pulse number into time (s), the *x*-axis should be multiplied by a factor of 0.033.

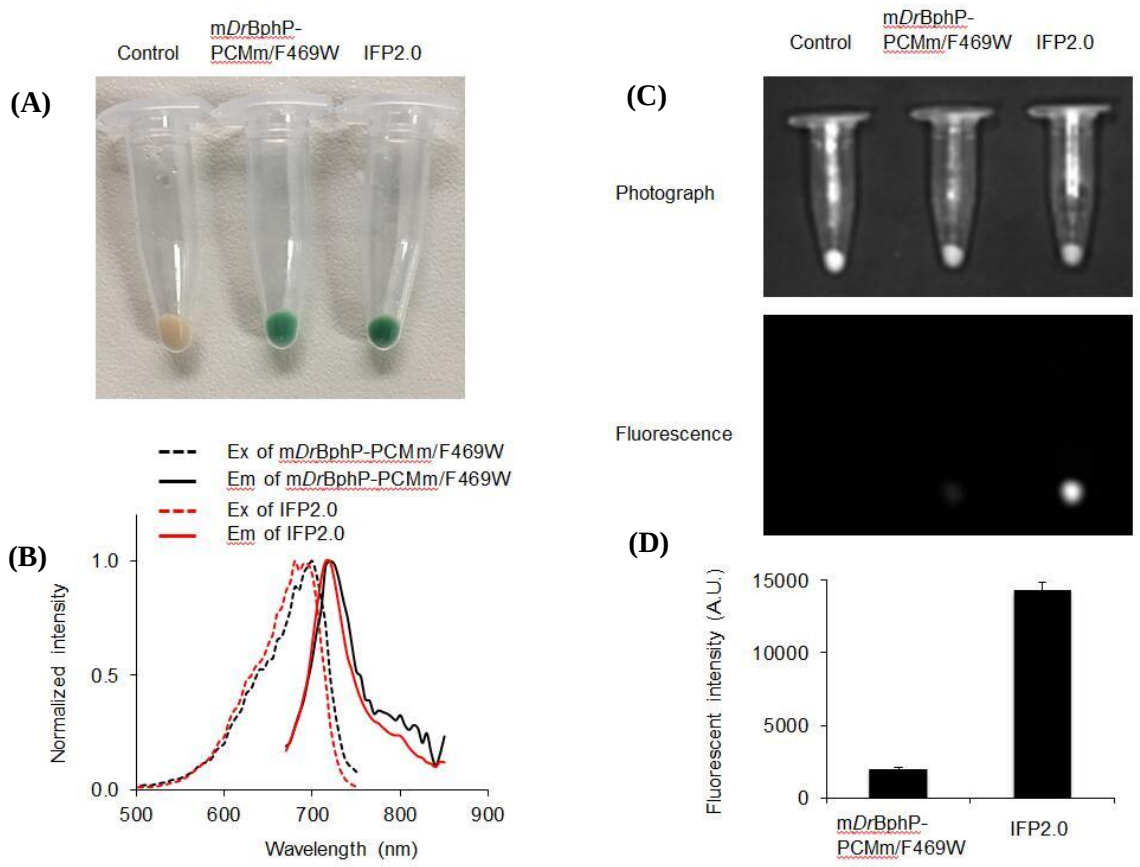

Fig. S3. Fluorescence properties of m*Dr*BphP-PCMm/F469W and its parent fluorescent protein miRFP2.0 in bacteria. (A) Bright-field images of bacterial cells expressing no fluorescent protein (control), m*Dr*BphP-PCMm/F469W and IFP2.0, respectively. The latter proteins were greenish in color, indicating good expression in bacteria. (B) Excitation (Ex) and emission (Em) spectra of m*Dr*BphP-PCMm/F469W and IFP2.0. (C) Fluorescent images of bacterial cells expressing no fluorescent protein (control), m*Dr*BphP-PCMm/F469W and IFP2.0, respectively. (D) Quantification of the fluorescent intensity of both m*Dr*BphP-PCMm/F469W and IFP2.0, showing that m*Dr*BphP-PCMm/F469W is 7 times dimmer than IFP2.0 in bacterial when excited at 675/30 nm. Data are presented as the mean ± standard error of mean (SEM). n = 3 preparations.

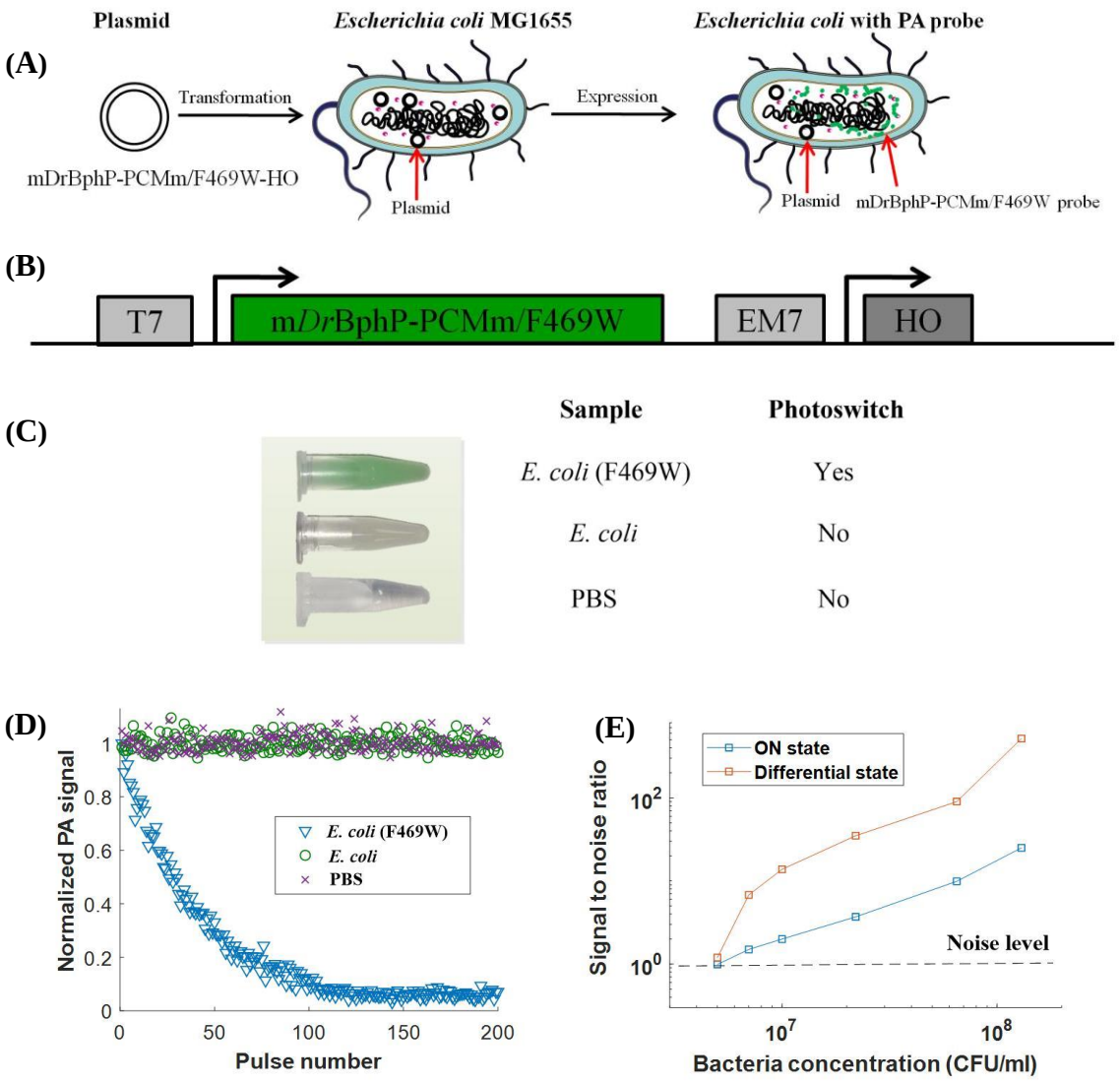

Fig. S4. Production of genetically encoded probes in *E. coli*. (A) *E. coli* M1655 were reprogrammed to express genetically encoded protein (m*Dr*BphP-PCMm/F469W) based on established genetic rules. (B) Schematic diagram of the gene structure: The expression of m*Dr*BphP-PCMm/F469W is controlled by the T7 promoter, and the expression of HO is controlled by the EM7 promoter. Arrows indicate the direction of translation. T7 promoter: the promoter of bacteriophage T7 RNA polymerase. EM7 promoter: constitutive synthetic prokaryotic promoter derived from the T7 promoter. HO: heme oxygenase. (C) Photograph of the supernatant of *E. coli* with and without expression of m*Dr*BphP-PCMm/F469W (i.e., *E. coli* (F469W) and *E. coli*), together with the photograph of PBS. Among the three samples, *E. coli* (F469W) exhibited a green color, indicating the expression of m*Dr*BphP-PCMm/F469W. (D) Normalized PA signals of *E. coli* (F469W), *E. coli* and PBS as a function of pulse number upon 780 nm illumination. Only *E. coli* (F469W) exhibited photoswitching. To convert the pulse number into time (s), the *x*-axis should be multiplied by a factor of 0.033. (E) PA SNR of *E. coli* (F469W) as a function of bacteria concentration (CFU/ml) for both ON and the differential states. *E. coli* (F469W) were embedded in a 10 mm thick scattering medium (0.1% intralipid).

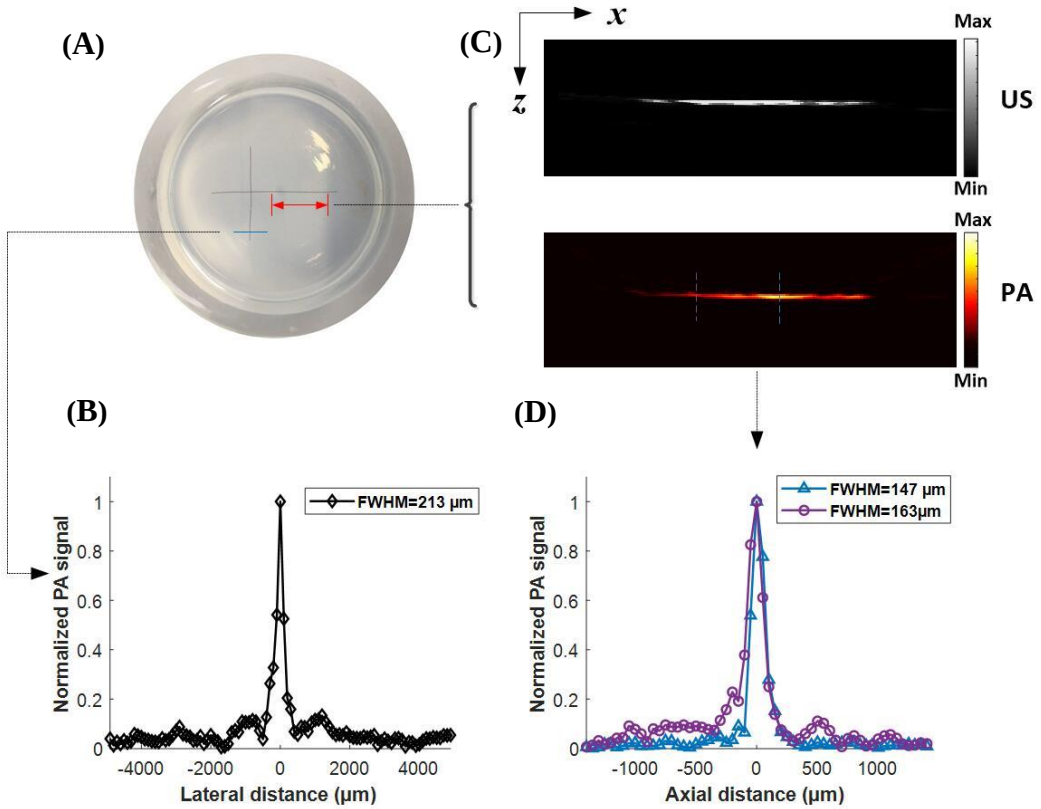

Fig. S5. Spatial resolution quantification of the PACT system. (A) A top-view photograph of two tungsten wires (30 μm diameter) fixed in agar gel. (B) The normalized PA signal profile along the blue line in (A). The results show a measured lateral resolution of approximately 213 μm. (C) Ultrasound (US) and PA Bscan of a tungsten wire target located at the red line shown in (A). The images were projected on the x-z plane. (D) The normalized PA signal profiles of the blue and purple dashed lines in the PA Bscan in (C). The results show a measured axial resolution of approximately 150 μm.

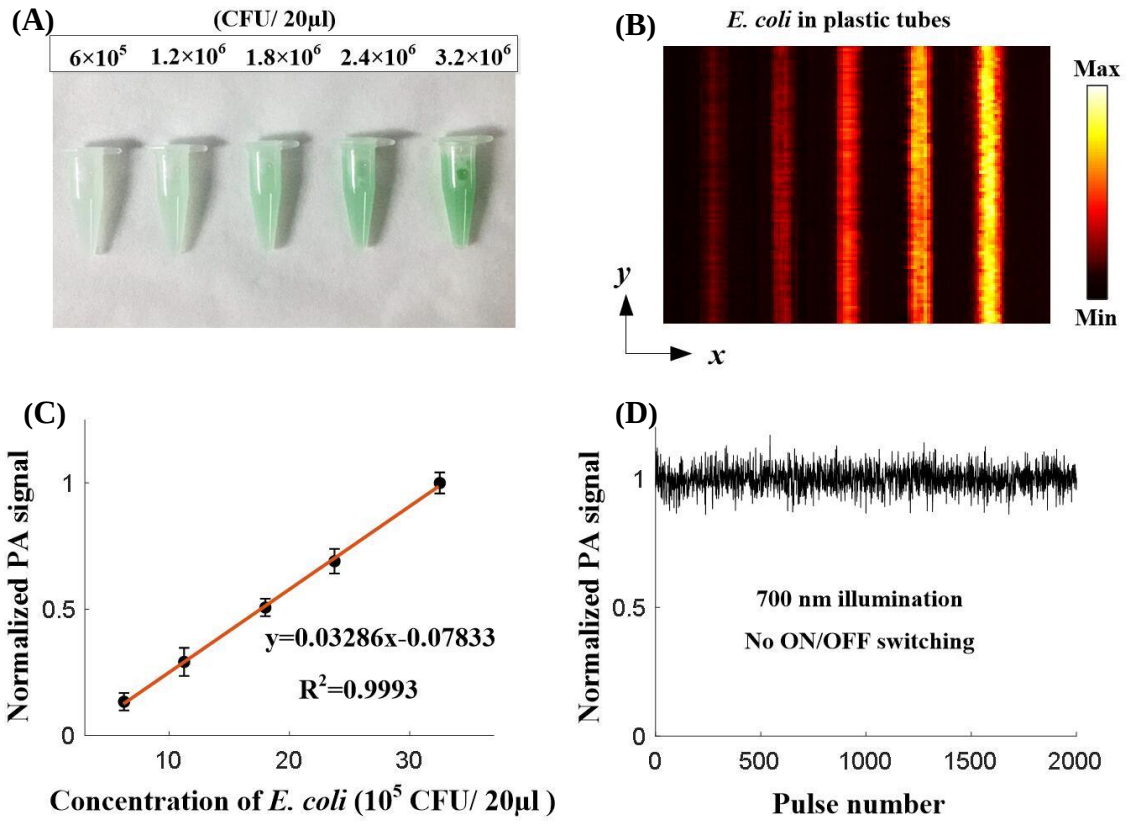

Fig. S6. PA properties of *E. coli* (F469W) at different bacteria concentrations (under 700 nm illumination). (A) Photographs of *E. coli* (F469W) supernatant at various bacterial concentrations ranging from 6 × 10^5 CFU/ 20μl to 3.2 × 10^6 CFU/ 20μl. (B) Corresponding maximum amplitude projection (MAP) PA images for the above *E. coli* (F469W) in plastic tubes. (C) Normalized PA signal as a function of bacterial concentration, in which the PA signal exhibits a linear correlation with bacterial concentration in the above range. Data are presented as the mean ± standard error. (D) Photostability of *E. coli* (F469W) after exposure to 2000 laser pulses. All data shown in this figure were obtained using 700 nm illumination without triggering the photoconversion of *E. coli* (F469W). To convert the pulse number into time (s), the *x*-axis should be multiplied by a factor of 0.033.

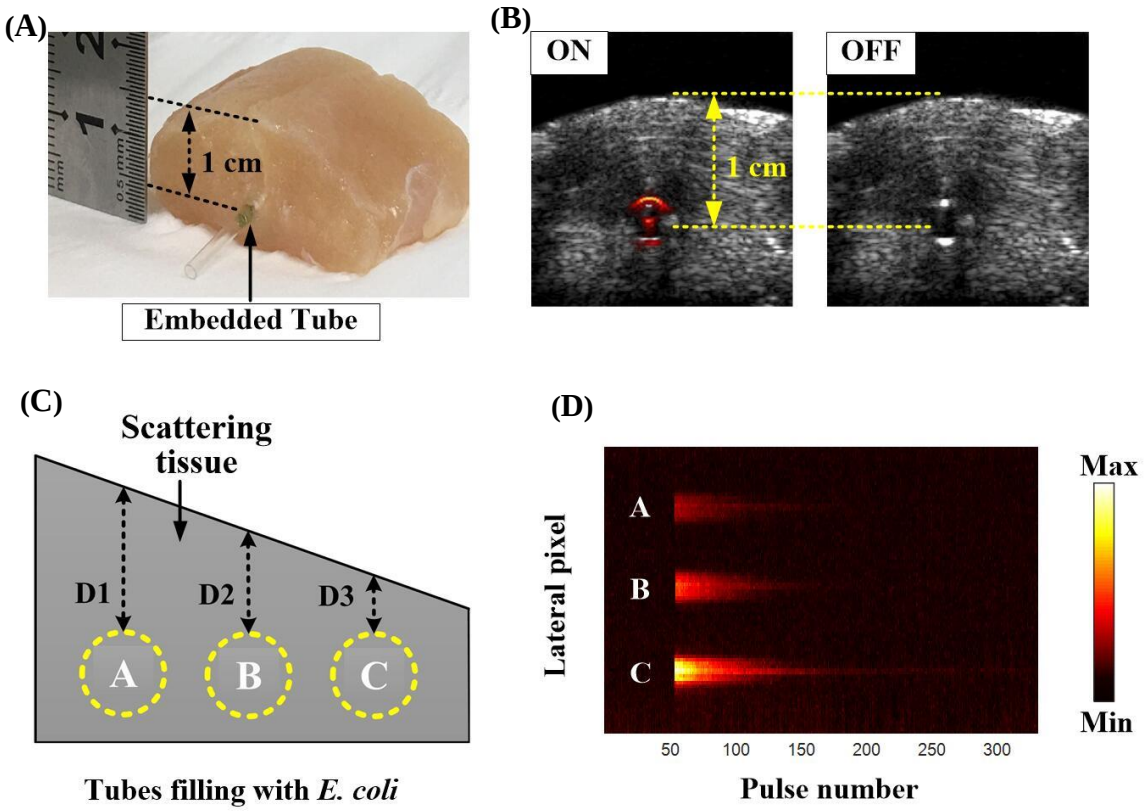

Fig. S7. Phantom PA test results of *E. coli* (F469W) at different depths of scattering tissues. (A) Photograph of a plastic tube filled with *E. coli* (F469W) embedded in chicken breast (1 cm thickness). (B) Corresponding photoacoustic Bscan of the above phantom in the ON and OFF states overlaid on the US image. The switching was induced by 780 nm photo-illumination. (C) Schematic diagram of tubes filled with *E. coli* (F469W) embedded in chicken breast at different depths (D1 = 1 cm, D2 = 0.8 cm and D3 = 0.5 cm). (D) Maximum amplitude projection (MAP) images of the same Bscan area of the above three tubes during 780 nm illumination plotted against time, i.e., pulse number (X-axis). The results show the variation in PA signals throughout the photoswitching process from the ON to OFF states at different depths in chicken breast. To convert the pulse number into time (s), the *x*-axis of the MAP image should be multiplied by a factor of 0.033.

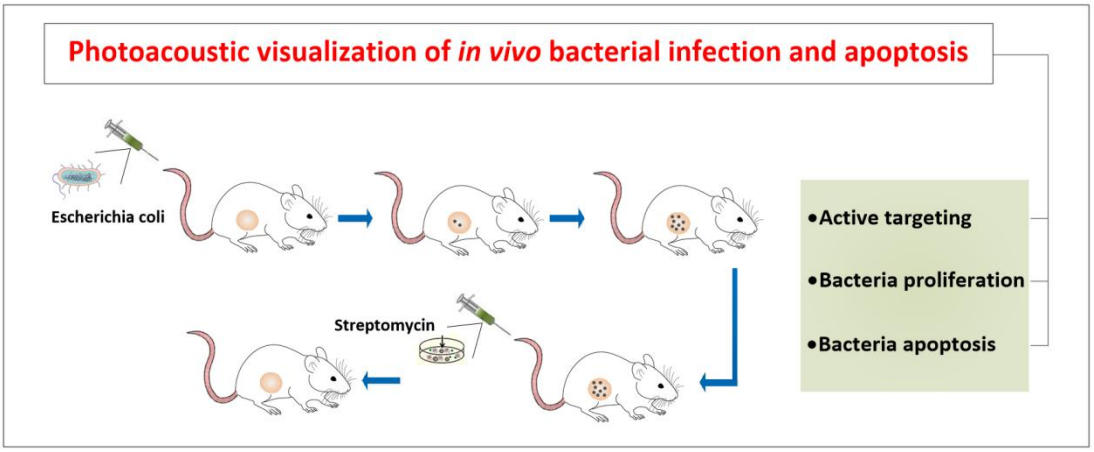

Fig. S8. Schematic illustration of tumor-targeted imaging based on the present bacterial delivery system.

Study group 1 (Mouse 1)

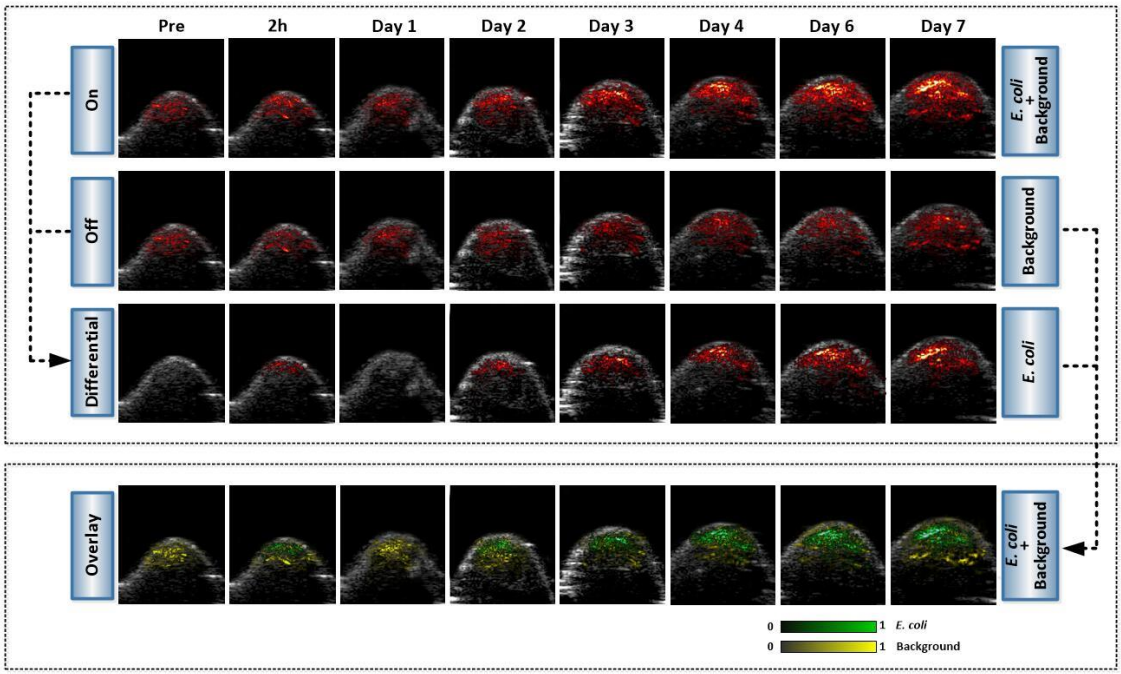

Study group 1 (Mouse 2)

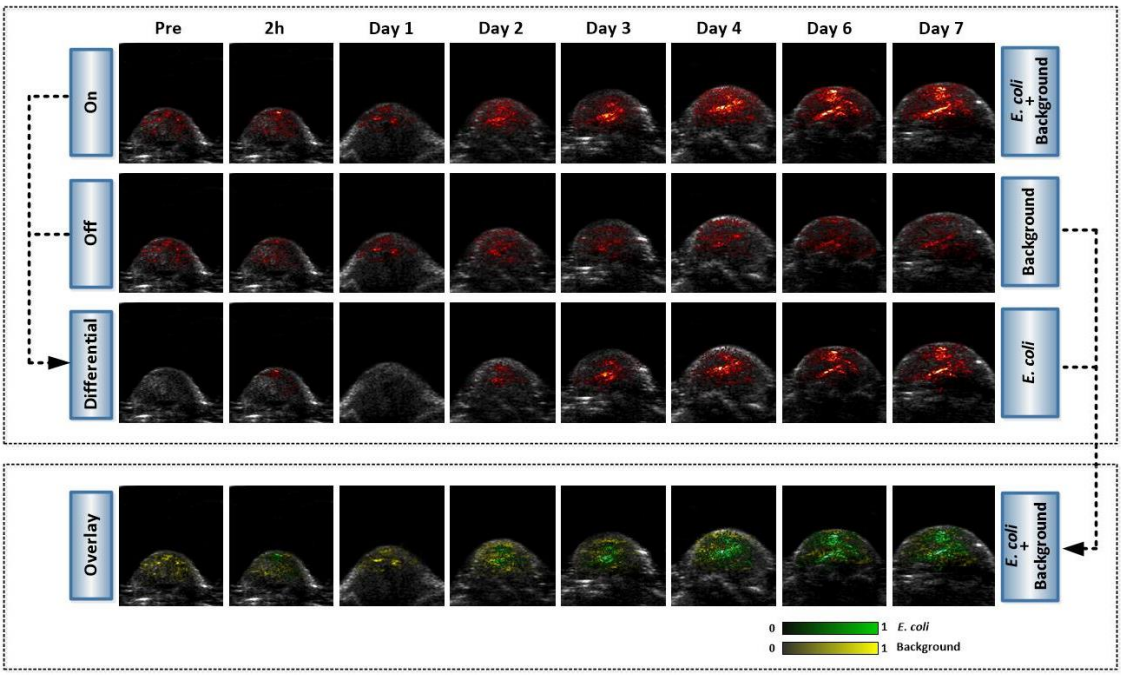

Study group 1 (Mouse 3)

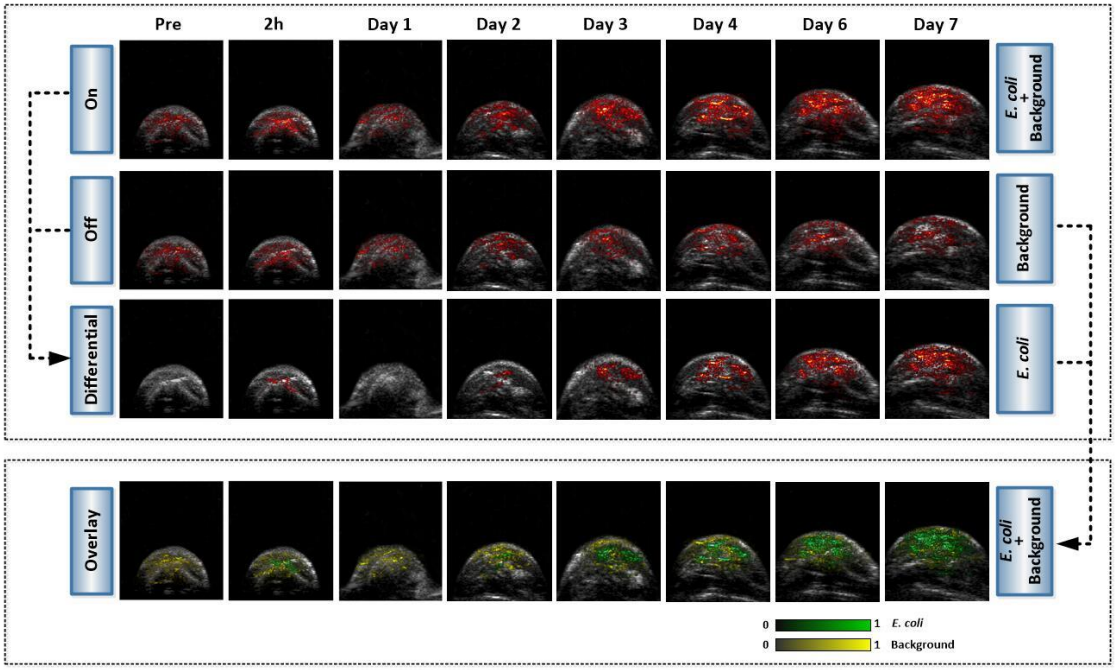

Study group 2 (Mouse 1)

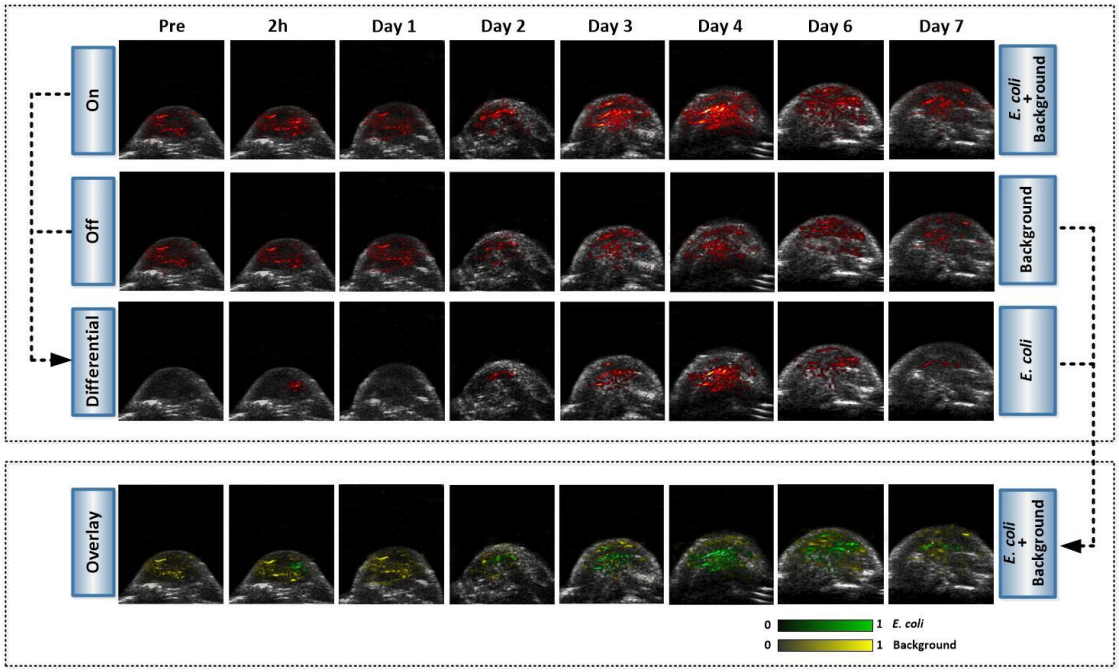

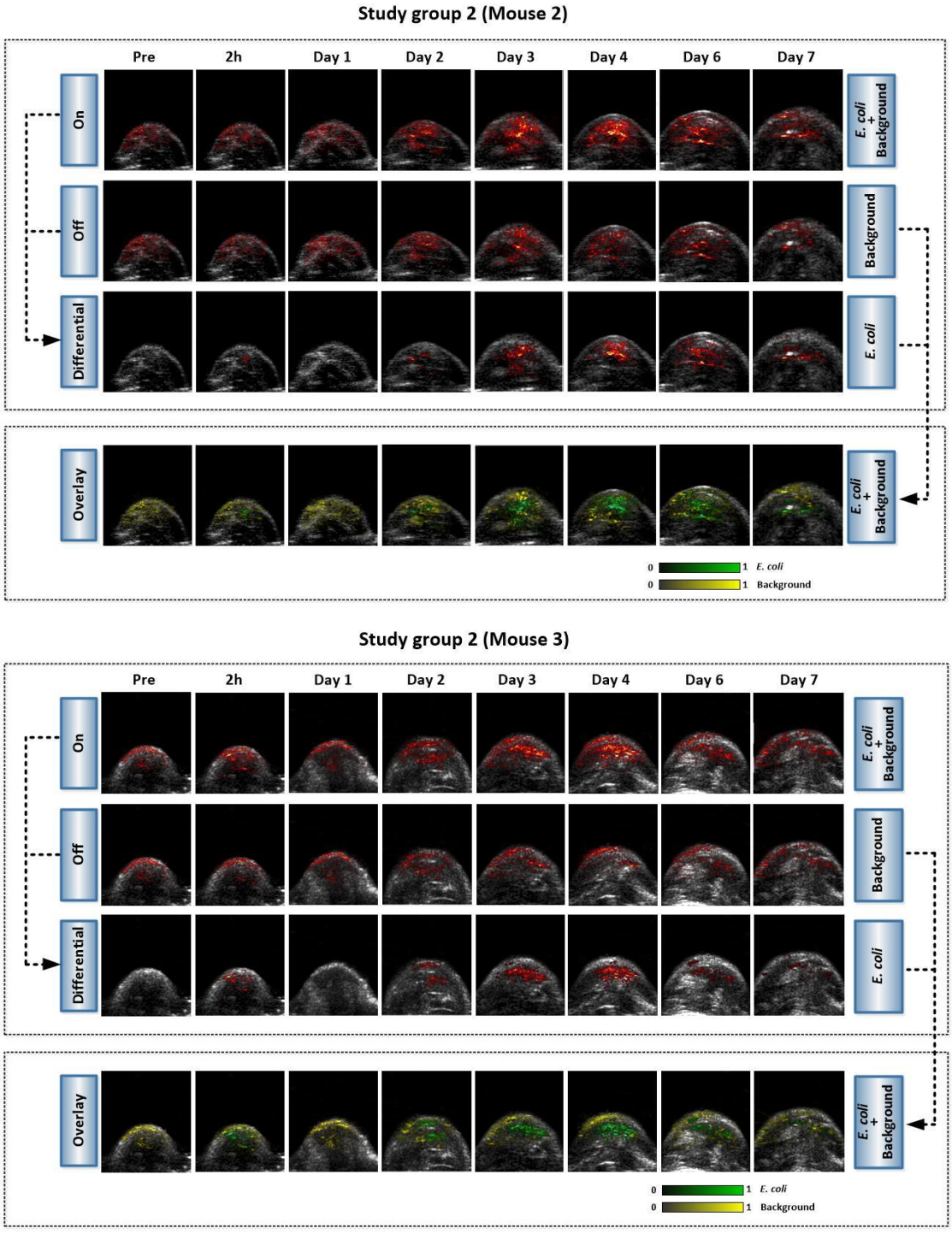

Fig. S9. *In vivo* PA imaging of mice in two study groups at different time points. In the overlay images, the extracted signals corresponding to *E. coli* are indicated in green, and the background signals including vasculature and skin melanin, etc. are indicated in yellow.

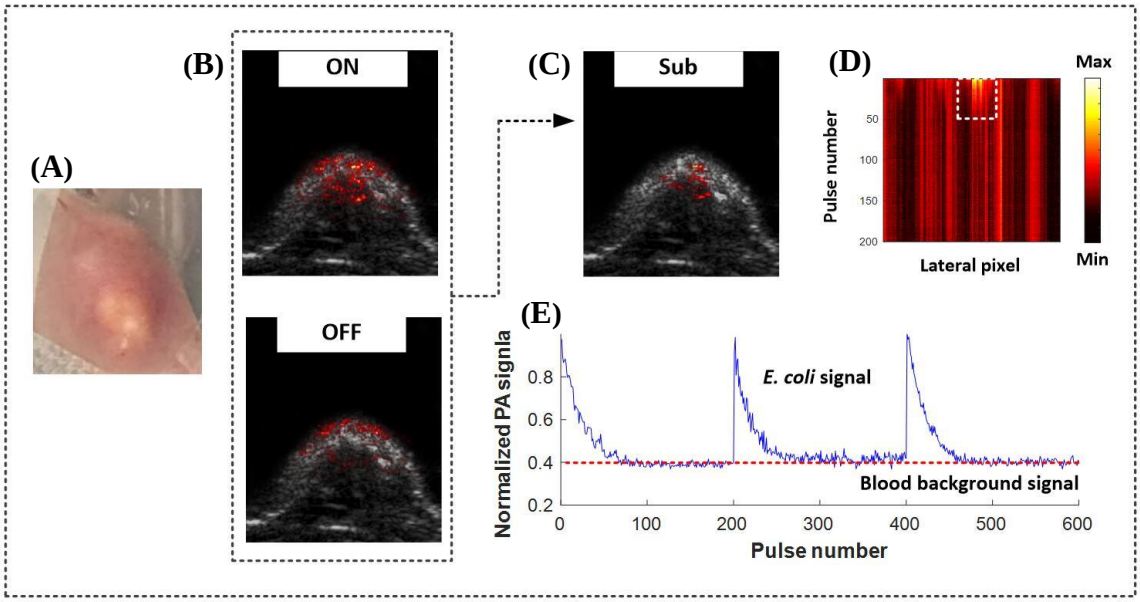

Fig. S10. *In vivo* PA imaging of mouse tumor regions (study groups) captured 2 h post-injection of the *E. coli* (F469W) used in this study. (A) Photograph of a representative mouse tumor region. (B) PA Bscan images of mouse tumor and nearby region in the ON and OFF states captured 2 h post-injection, overlaid on the corresponding US image. (C) Subtracted Bscan between ON and OFF states, showing the signal of *E. coli* (F469W). (D) Maximum amplitude projection (MAP) images of the same Bscan area plotted against time. The results reveal the change in the PA signal from the ON to OFF states. (E) Multiple cycles of the photoswitching process at 2 h post-injection, validating the reversible photoswitching performance of *E. coli*, as well as the reproducibility of the PA imaging outcomes at 2 h post-injection. To convert the pulse number into time (s), the *y*-axis of MAP images in (D) and *x*-axis in (E) should be multiplied by a factor of 0.033.

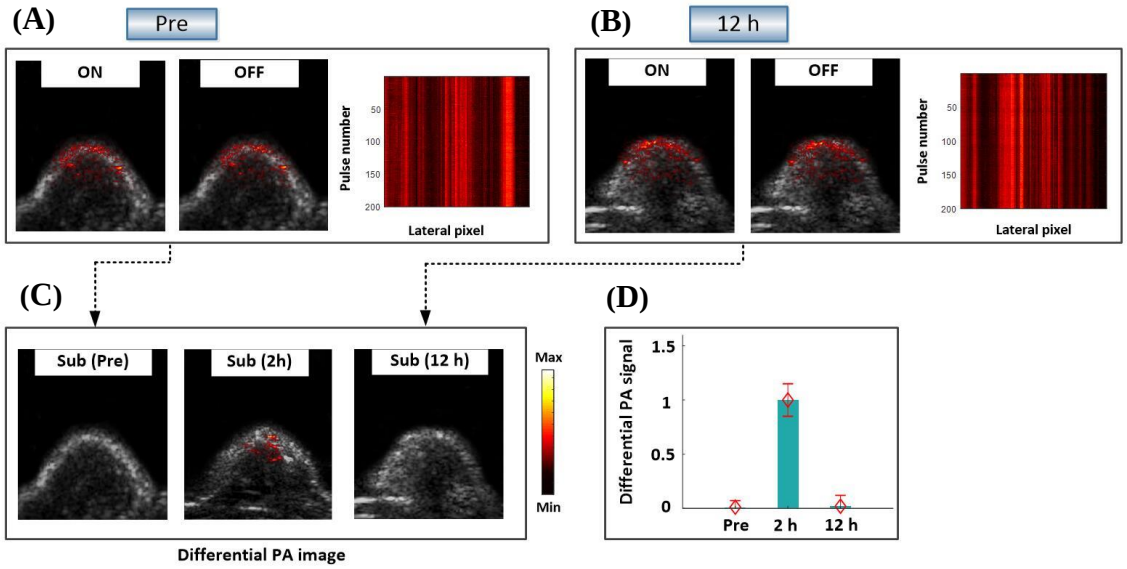

Fig. S11. Clearance of *E. coli* (F469W) from the circulatory system over the course of 12 h. (A) PA results prior to the intravenous injection of *E. coli*. (B) PA images recorded 12 h post-injection of *E. coli.* The above results include Bscan images in both the ON and OFF states, as well as MAP images of the same Bscan area plotted against time. The MAP images indicate no obvious change in the PA signal upon irradiation at 780 nm for both Pre and 12 h images. To convert the pulse number into time (s), the *y*-axis of MAP images in (A) and (B) should be multiplied by a factor of 0.033. (C) Differential PA images pre-injection and 2- and 12-h post-injection of *E. coli*. The results indicate a half-life of 12 h for the clearance of intravenously injected *E. coli* from blood circulation. PA imaging outcomes 2 h post-injection are shown in Supplementary Figure 10. (D) Statistical results of the *E. coli* signal in the tumor region at the above time points. Data are presented as the mean $\pm$ standard error (n = 3).

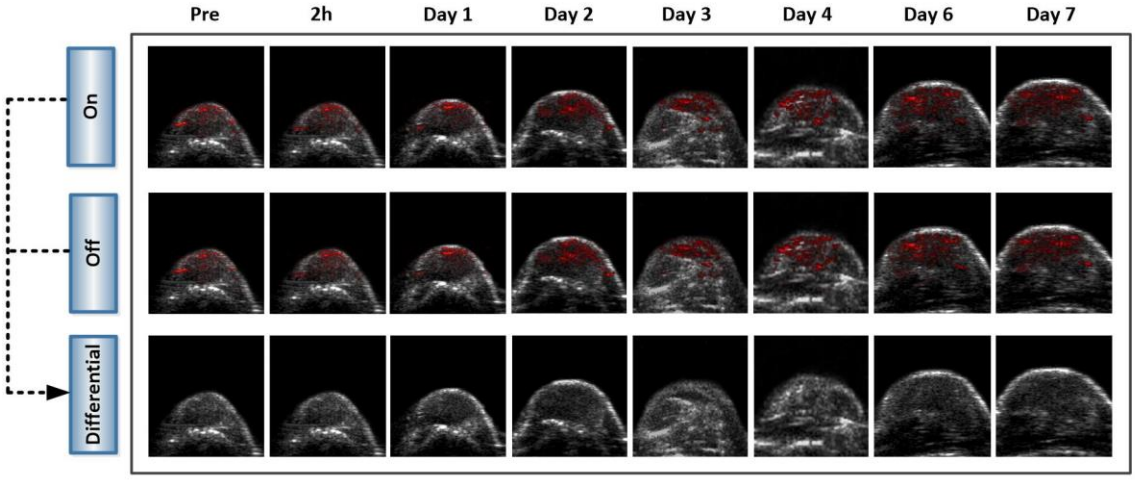

Fig. S12. *In vivo* PA imaging of representative mice in the control group at different time points.

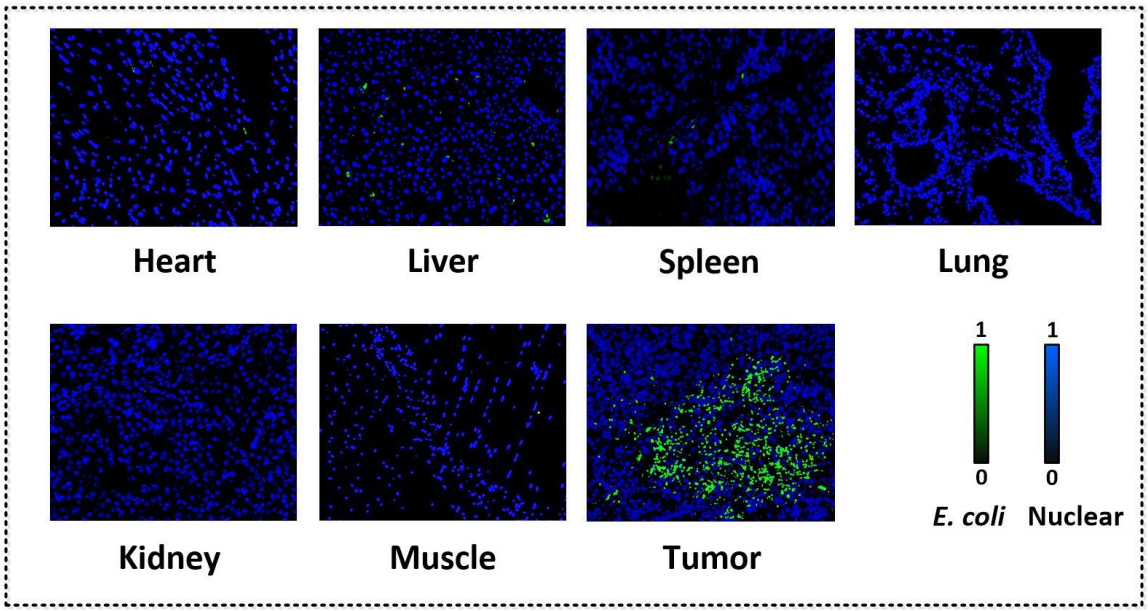

Fig. S13. Representative FISH images of major organs, muscle tissue and tumor region, collected from mice sacrificed 7 days post-injection with *E. coli* (F469W).

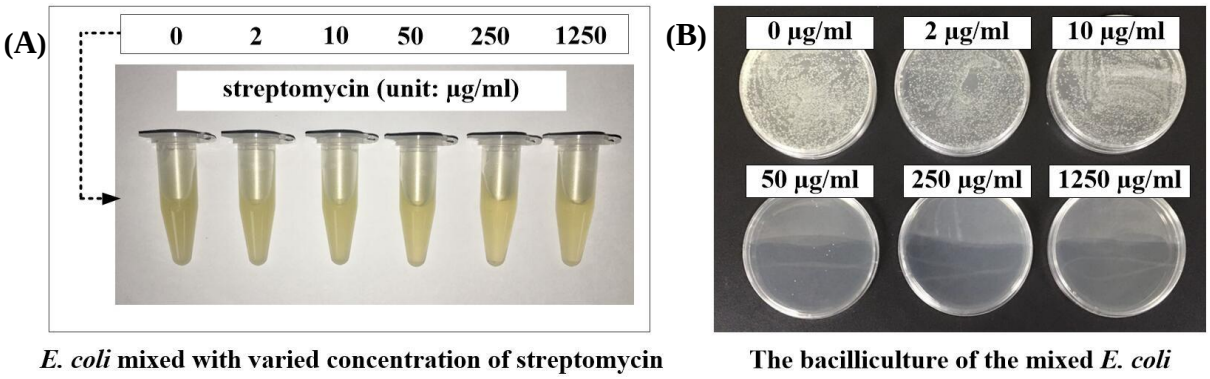

E. coli mixed with varied concentration of streptomycin

The bacilliculture of the mixed *E. coli*

Fig. S14. *In vitro E. coli*-killing effect of streptomycin at different concentrations. (A) EP tubes filled with *E. coli* MG1655 (1 ml) containing different concentrations of streptomycin. (B) After being diluted 10,000 times, the *E. coli* in each of these tubes were then transferred to bacteriological culture dishes for bacilliculture. The different viabilities of *E. coli* in the dishes reflect different bacteria-killing effects of streptomycin at various concentrations. The results support the conclusion that *E. coli* does not reproduce after being treated with ≥50 μg/ml of streptomycin, which can be viewed as the approximate minimum effective dose for *E. coli* killing (1 ml or equivalent OD).

Table S1. Absorption states and photoswitching properties of different purified proteins.

Protein	Absorbance @780 nm ($M^{-1}cm^{-1}$) ON State	Absorbance @780 nm ($M^{-1}cm^{-1}$) OFF State	Photoswitching ratio @780 nm (absorbance) [a]	Photoswitching ratio @780 nm (photoacoustic) [b]
m*Dr*BphP-PCMm/F469W	35436.8	2216.2	15.99	17.17
m*Dr*BphP-PCMm/L463R	35035	4325.3	8.10	8.25
m*Dr*BphP-PCMm	24519.6	2581.0	9.50	10.42
*Dr*BphP-PCM	21893.2	2392.7	9.15	8.94
RpBphP1	15013.6	3950.9	3.80	4.15

[a] The photoswitching ratio (absorbance) refers to absorbance (ON)/absorbance (OFF).

[b] The photoswitching ratio refers to PA (ON) /PA (OFF). The results originate from the photoacoustic characterization of proteins (Fig. S1D and E).

SI References

1. Auldridge, M.E., K.A. Satyshur, D.M. Anstrom, and K.T. Forest, *Structure-guided Engineering Enhances a Phytochrome-based Infrared Fluorescent Protein.* Journal of Biological Chemistry, 2012. **287**(10): p. 7000-7009.
2. Burgie, E.S., J. Zhang, and Richard D. Vierstra, *Crystal Structure of Deinococcus Phytochrome in the Photoactivated State Reveals a Cascade of Structural Rearrangements during Photoconversion.* Structure, 2016. **24**(3): p. 448-457.
3. Xu, M. and L.V. Wang, *Universal back-projection algorithm for photoacoustic computed tomography.* Physical Review E, 2005. **71**(1): p. 016706.